Phase and solute fields across the solid-liquid interface of a binary alloy

Massimo Conti
Dipartimento di Matematica e Fisica, Università di Camerino and Istituto Nazionale di Fisica della Materia, Via Madonna delle Carceri, I-62032 Camerino, Italy

(Received 22 January 1999; revised manuscript received 24 March 1999)

Solidification of binary alloys is characterized by a sharp structural transition across the solid-liquid interface. It is a typical situation which suggests a nonlocal dependence of the appropriate thermodynamic potential on its associate fields. Phase-field models with a gradient contribution for the order parameter have proved to account for nonequilibrium effects, as solute trapping and kinetic undercooling of the solid-liquid interface. The inclusion of a gradient term for the concentration field has also been theoretically investigated, but in this case the correspondence between predicted phenomena and experimental results is still rather unexplored. In the present study we analyze numerical solutions of a phase-field model in both steady and transient conditions. We focus on effects which are critically dependent on the composition field across the solid-liquid interface; the extent of the concentration gradient correction is related to measurable quantities to suggest methods for a comparison between the model predictions and experimental data. [S1063-651X(99)01108-3]

PACS number(s): 64.70.Dv, 68.10.Gw, 81.30.Bx, 82.65.Dp

I. INTRODUCTION

Rapid solidification of binary alloys is addressed through sharp interface or phase-field models. Sharp interface models [1,2] utilize the diffusion equation to describe the transport of heat and solute through the bulk phases. The matching conditions at the interface boundary reflect (i) conservation constraints for energy and solute and (ii) constitutive laws that relate the local interface concentration c and temperature T to the front velocity v. The latter require a separate modellization of the interface kinetics on a microscopic scale. Aziz and Kaplan [3] and Aziz and Boettinger [4] addressed this point within the continuous growth model (CGM), assuming isothermal and steady conditions: they argued that the solute redistribution across the solid-liquid interface is driven by a diffusional mechanism characterized by a velocity scale $v_d \sim D/a$, where D is the interface solute diffusivity and a is a length representative of the interface thickness; as the front velocity becomes of the order of v_d, this mechanism becomes less effective and the partition coefficient $k(v)$ (i.e., the ratio c_s/c_l of solute concentration in the growing solid to that in the liquid at the interface) deviates from the equilibrium value k_e, increasing towards unity at large growth rates. This phenomenon, well known in rapid solidification experiments, is termed *solute trapping*. It is worth noting that the above argument implies an intrinsically ''finite-thickness'' interface, whereas the diffusional model requires boundary conditions on a zero-dimensional interface. This is a rather delicate issue in rapid solidification processes when the solute diffusion length becomes of the order of atomic dimensions (i.e., $D/v \sim a$).

Within the phase-field model (PFM) an order parameter $\phi(x,t)$ characterizes the phase of the system at each point; a free-energy (or entropy) functional, depending on ϕ, T, and c and including gradient correction terms, is then extremized in respect to these variables to derive the dynamic equations for the process. Wheeler, Boettinger, and McFadden (WBM1) [5] were the first to apply the PFM to alloy solidification in the isothermal limit. They started from a Landau-Ginzburg free-energy functional depending on the bulk free-energy density and including a $(\nabla\phi)^2$ term. In their study an asymptotic analysis was conducted to demonstrate that the model recovers the classical sharp interface formulation when the interfacial layer is sufficiently thin; moreover, the characteristic parameters of the PFM were related to the actual material properties. However, in their analysis the partition coefficient k resulted a decreasing function of the front velocity, and the authors concluded that the model was unable to predict solute trapping. The same conclusion could be drawn from the sharp interface limit of a slightly different model proposed by Caginalp and Jones [6]. In a succeeding study Wheeler, Boettinger, and McFadden (WBM2) [7] recovered the correct dependence $k(v)$ through the inclusion in the free-energy functional of a $(\nabla c)^2$ term, acting to oppose the contraction of the solute profile at large velocities. As shown by Bi and Sekerka [8], this new version of the model is the limiting case of a more general thermodynamic formulation which contains square gradient terms in all the associate fields of a suitable entropy functional and admits coupling effects between phenomena of equal tensorial rank. Retaining the $(\nabla c)^2$ term, the surface free-energy excess reduces to the values of the surface tension of the pure solvent or solute at $c=0$ and $c=1$, respectively, exhibiting a maximum in between [7,9]. At low solute concentration, this behavior seems to be in qualitative agreement with some experimental results; however, the lack of reliable experimental data makes the validation of the model very hard. A more intriguing perspective was achieved when it was realized that the $(\nabla c)^2$ term is not necessary to predict solute trapping [10,11]: this phenomenon naturally disappears in the sharp interface limit of the model studied by WBM1, but is fully recovered taking into account the finite thickness of the interface. Neglecting the $(\nabla c)^2$ contribution, in a further investigation Ahmad *et al.* [11] were able to show that even the free-energy dissipation in the interfacial region due to *solute drag* naturally arises from the model equations; moreover, they pointed out that solute trapping is critically dependent on the modeling of the solute diffusivity in the interfacial region. Then, at present, no decisive arguments are available to assess whether and to what extent a gradient

concentration term is necessary for a proper description of the interfacial dynamics.

In the present study we address the rapid solidification of an ideal binary alloy through a phase-field model which incorporates both the $(\nabla\phi)^2$ and $(\nabla c)^2$ terms. The model is solved numerically in directional solidification conditions: the solidification process is driven by a moving temperature field, neglecting the effect of the latent heat diffusion. The aim of our investigation is to focus on effects which are critically dependent on the composition field across the solid-liquid interface in order to relate predictable phenomena and measurable quantities with the extent of the concentration gradient correction. As the latter causes a stretching of the solute profile, we found that it reflects essentially on the solute relaxation time across the interface, decreasing the value of the diffusional velocity v_d. Then the onset of solute trapping is shifted towards lower velocities in a predictable way. Moreover, the dependence of the interface temperature on the interface velocity is also affected, resulting in a shift of the parameters region where oscillatory instabilities of the solidification front can be expected.

The paper is organized as follows: In Sec. II the governing equations of the model will be derived through the extremization of an entropy functional. In Sec. III some details of the numerical method will be given, and in Sec. IV the results of the numerical simulations will be discussed. The conclusions will follow in Sec. V.

II. GOVERNING EQUATIONS

The model directly follows the formulation given by Warren and Boettinger [12] for isothermal solidification: full details of the derivation are presented in that reference. The total entropy of an ideal solution of components A (solvent) and B (solute) is written as

$$\mathcal{S}=\int\left[s(e,\phi,c)-\frac{\epsilon^2}{2}|\nabla\phi|^2-\frac{\delta^2}{2}|\nabla c|^2\right]dv, \tag{1}$$

where integration is performed over the system volume; s is the thermodynamic entropy density that depends on the internal energy density e and on the concentration and phase fields; the coefficients ϵ and δ describe the extent of the gradient term corrections. The phase field ϕ assumes the values $\phi=0$ in the solid and $\phi=1$ in the liquid; intermediate values correspond to the interface between the two phases. To ensure a positive local entropy production, the governing equations for the phase and solute fields can be written as

$$\dot{\phi}=M_\phi\frac{\delta\mathcal{S}}{\delta\phi}, \tag{2}$$

$$\dot{c}=-\nabla\cdot\left(M_c\nabla\frac{\delta\mathcal{S}}{\delta c}\right), \tag{3}$$

where M_c and M_ϕ are positive constants. For the pure species A and B, the bulk free-energy density is postulated to be of the form;

$$f^{A,B}(\phi,T)=TG^{A,B}(\phi)+p(\phi)L^{A,B}\left(1-\frac{T}{T^{A,B}}\right)-CT\ln\left(\frac{T}{T^{A,B}}\right), \tag{4}$$

where $G^{A,B}=(1/4)\tilde{W}^{A,B}\phi^2(1-\phi)^2=\tilde{W}^{A,B}g(\phi)$ is a symmetric double-well potential with equal minima at $\phi=0$ and $\phi=1$, scaled by the positive well height $\tilde{W}^{A,B}$; $T^{A,B}$ and $L^{A,B}$ represent the melting temperature and the latent heat per unit volume of the pure species A or B. For the specific heat C we assume constant and equal values for both phases and materials. Choosing the function $p(\phi)$ as $p(\phi)=\phi^3(10-15\phi+6\phi^2)$, the condition is enforced that bulk solid and liquid are described by $\phi=0$ and $\phi=1$, respectively, for every value of the temperature [13]. For an ideal solution the chemical potentials of the solvent and solute are given by

$$\mu^A=f^A(\phi,T)+\frac{RT}{v_m}\ln(1-c), \tag{5}$$

$$\mu^B=f^B(\phi,T)+\frac{RT}{v_m}\ln(c). \tag{6}$$

Here R is the gas constant and v_m is the molar volume. The bulk free energy density of the solution is assumed as $f=(1-c)\mu^A+c\mu^B$; then, recalling that $-T(\partial s/\partial\phi)=\partial f/\partial\phi$ and taking the functional derivatives in Eqs. (2) and (3) yields

$$\frac{\partial\phi}{\partial t}=M_\phi[\epsilon^2\nabla^2\phi-(1-c)\tilde{H}^A(\phi,T)-c\tilde{H}^B(\phi,T)], \tag{7}$$

$$\frac{\partial c}{\partial t}=-\nabla\cdot\left\{D_c c(1-c)\frac{v_m}{R}[\tilde{H}^A(\phi,T)-\tilde{H}^B(\phi,T)]\nabla\phi-D_c\nabla c+D_c c(1-c)\frac{v_m}{R}\tilde{\Gamma}(\phi,T)\nabla T+D_c c(1-c)\frac{v_m}{R}\nabla(\delta^2\nabla^2 c)\right\}, \tag{8}$$

with

$$\tilde{H}^{A,B}(\dot{\phi},T)=\tilde{W}^{A,B}\frac{dg(\phi)}{d\phi}-\frac{dp(\phi)}{d\phi}L^{A,B}\frac{T-T^{A,B}}{TT^{A,B}}, \tag{9}$$

$$\tilde{\Gamma}(\phi,T)=-\frac{p(\phi)}{T^2}(L^A-L^B). \tag{10}$$

In Eq. (8) the standard definition of the solute diffusivity D_c has been recovered, taking

$$D_c=\frac{M_c}{c(1-c)}\frac{R}{v_m}. \tag{11}$$

To allow for different diffusivities in the solid and liquid phases, in the following D_c will be taken as $D_c=D_s+p(\phi)(D_l-D_s)$, D_l and D_s being the diffusivities in the liquid and in the solid, respectively. Notice that in [12] the contribution of $(\nabla c)^2$ in Eq. (1) is neglected, setting $\delta=0$, and, dealing with isothermal solidification, on the right-hand side of Eq. (8) only the first two terms are retained.

As we neglect the latent heat diffusion, the temperature field is decoupled from the phase and concentration fields, and is represented as a traveling wave moving towards the

positive x direction with uniform gradient $\tilde{G}$ and constant velocity $\tilde{V}_0$:

$$\frac{\partial T}{\partial t} = -\tilde{V}_0 \frac{\partial T}{\partial x} = -\tilde{V}_0 \tilde{G}. \tag{12}$$

The problem will be treated by scaling lengths to some reference length ξ and time to ξ^2/D_l. We allow M_ϕ to depend on the local composition as $M_\phi = (1-c)M_\phi^A + cM_\phi^B$. To associate the model parameters to the material properties of the alloy, we follow the method suggested by Warren and Boettinger [12], based on the analysis of the sharp interface limit of the model, though in the present case the contribution of $(\nabla c)^2$ in Eq. (1) could affect to some extent the results of their analysis. Then the governing equations become

$$\frac{\partial \phi}{\partial t} = [(1-c)m^A + cm^B][\nabla^2 \phi + (1-c)Q^A(T,\phi) + cQ^B(T,\phi)], \tag{13}$$

$$\frac{\partial c}{\partial t} = -\nabla \cdot \{c(1-c)\lambda(\phi)[H^A(\phi,T) - H^B(\phi,T)]\nabla \phi + c(1-c)\lambda(\phi)\Gamma(\phi,T)\nabla T + c(1-c)\lambda(\phi)\nabla(E\nabla^2 c) - \lambda(\phi)\nabla c\}, \tag{14}$$

$$\frac{\partial T}{\partial t} = -V_0 \frac{\partial T}{\partial x} = -V_0 G, \tag{15}$$

where in Eq. (14) we put $E = (\nu_m \delta^2)/(R\xi^2)$, $H^{A,B}(\phi,T) = (\nu_m/R)\tilde{H}^{A,B}(\phi,T)$, $\Gamma(\phi,T) = (\nu_m/R)\tilde{\Gamma}(\phi,T)$, and $\lambda(\phi) = D_s/D_l + p(\phi)(1 - D_s/D_l)$. In Eq. (15) we define $V_0 = \tilde{V}_0 \xi/D_l$ and $G = \tilde{G}\xi$. The function $Q^{A,B}(\phi,T)$ is defined as

$$Q^{A,B}(\phi,T) = -\frac{\xi^2}{(h^{A,B})^2}\frac{dg(\phi)}{d\phi} + \frac{1}{6\sqrt{2}}\frac{\xi^2 L^{A,B}}{\sigma^{A,B} h^{A,B}}\frac{T - T^{A,B}}{\overline{T_I}}\frac{dp(\phi)}{d\phi}, \tag{16}$$

where $\sigma^{A,B}$ and $h^{A,B}$ indicate the surface tension and the interface thickness of the pure components A and B, respectively; $\overline{T_I}$ is the initial (equilibrium) interface temperature. The model parameters $m^{A,B}$ and $\tilde{W}^{A,B}$ depend on the physical properties of the alloy components through

$$m^{A,B} = \frac{\beta^{A,B}\sigma^{A,B}T^{A,B}}{D_l L^{A,B}}, \quad \tilde{W}^{A,B} = \frac{12}{\sqrt{2}}\frac{\sigma^{A,B}}{T^{A,B}h^{A,B}}, \tag{17}$$

where $\beta^{A,B}$ is the kinetic undercooling coefficient of pure A or B, which relates the interface undercooling to the interface velocity v through $v = \beta^{A,B}(T^{A,B} - T_I)$.

To estimate the above parameters we referred to the thermophysical properties of nickel (solvent) and copper (solute), summarized in Table I. The solute diffusivity in the solid phase was estimated as $D_s = 10^{-6} D_l$. The length scale was fixed at $\xi = 2.1 \times 10^{-4}$ cm; the kinetic undercooling coefficients were fixed to $\beta^A = 128.64\ \mathrm{cm\,s^{-1}\,K^{-1}}$ and $\beta^B = 153.60\ \mathrm{cm\,s^{-1}\,K^{-1}}$, not far from the actual best estimates [14], and a realistic value for the interface thickness was selected as 1.68×10^{-7} cm. With these values, $\tilde{W}^A = 1.082$, $\tilde{W}^B = 1.079$, and $m^A = m^B = 350$ result.

TABLE I. Material parameters for the Ni-Cu alloy.

Parameter	Nickel	Copper
T_m (K)	1728	1358
L (J/cm^3)	2350	1728
ν_m (cm^3/mol)[a]	7.0	7.8
σ (J/cm^2)	3.7×10^{-5}	2.8×10^{-5}
β (cm/K s)[b]	160	198
D_l (cm^2/s)	10^{-5}	10^{-5}

[a]An average value of 7.4 will be taken.
[b]From the estimation of Willnecker *et al.* [14].

III. NUMERICAL METHOD

The evolution of Eqs. (13)–(15) has been considered in one spatial dimension, in the domain $0 \leq x \leq x_m$, with x_m large enough to prevent finite-size effects. Fluxless boundary conditions for ϕ, c and transparent conditions for T were imposed at the domain walls. The initial temperature profile was defined as

$$T(x,0) = \overline{T_I} + G(x - x_0), \tag{18}$$

with a phase boundary at temperature $\overline{T_I}$ separating the solid region ($x < x_0$, $\phi = 0$) and the liquid region ($x > x_0$, $\phi = 1$). The interface was prepared in equilibrium conditions, with the initial solute concentration in the two phases corresponding to the equilibrium values at $\overline{T_I}$. Then the temperature profile was pulled towards the positive x direction, starting the solidification process.

To discretize the equations of the model second order in space and first order in time, finite-difference approximations were utilized; then, an explicit scheme was employed to advance the solution forward in time. As we did not use adaptive techniques, the entire grid was resolved at the same scale. The choice of the computational grid posed some delicate problems. The mesh spacing Δx has to be selected low enough to ensure an accurate resolution of both the phase-field and concentration profiles in the interfacial region. The fourth-order concentration equation (14) requires, for numerical stability, a time step Δt_c which scales as $(\Delta x)^4$. On the other hand, the phase-field equation (13) is a diffusion-reaction equation with diffusivity $D_\phi = m^{A,B} = 350$; in this case, the time step for stability, Δt_ϕ, is expected to scale as $(\Delta x)^2$ and, in one dimension, must be chosen at least lower than $(\Delta x)^2/(2D_\phi)$. Because of the large value of D_ϕ, in most of the simulations we found $\Delta t_\phi < \Delta t_c$. At least in principle, to save computational effort, the two equations could be resolved with different time steps (i.e., iterating the equation with smaller Δt within a single time step of the

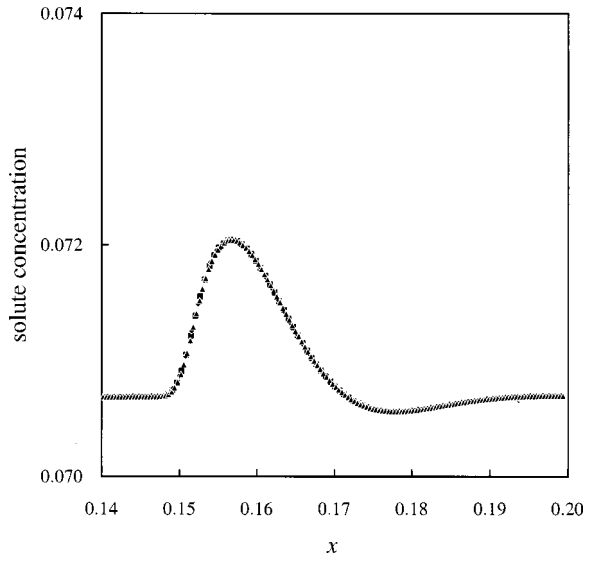

FIG. 1. Concentration profile for $\epsilon/\delta=0.025$, calculated with three different values of the grid spacing Δx: $\Delta x=8\times10^{-4}$ (diamonds), $\Delta x=6\times10^{-4}$ (squares), and $\Delta x=4\times10^{-4}$ (triangles). $V_0=500$ and $G=200$ K.

equation with larger Δt); however, we decided to use the smallest of Δt_ϕ and Δt_c for both equations.

Previous studies conducted in one or two dimensions indicate that accurate solutions can be obtained choosing a grid spacing of the order of the nominal interface thickness $\tilde{h}^{A,B}=h^{A,B}/\xi$. In our simulations we have $\tilde{h}^{A,B}=8\times10^{-4}$. We observed that to avoid spurious instabilities of the growth rate the maximum Δx allowed was $\Delta x=6\times10^{-4}$ for $\epsilon/\delta>0.1$; at lower values of ϵ/δ, the stretching of the solute profile in the interfacial region allowed us to use a value of $\Delta x\leqslant8\times10^{-4}$. Convergence of the numerical results was checked for both low and large values of ϵ/δ. Figure 1 shows the solute profile for $\epsilon/\delta=0.025$, $V_0=500$, and $G=200$ K. The initial concentration of the alloy is $c_{-\infty}=0.056\,09$ in the solid phase and $c_{+\infty}=0.070\,68$ in the liquid phase, corresponding to an equilibrium temperature $\overline{T_I}=1706.06$ K. The picture is taken at $t=2.5\times10^{-4}$, when the growth process reached a steady regime. The three sets of data refer to different values of Δx, i.e., $\Delta x=8\times10^{-4}, 6\times10^{-4}, 4\times10^{-4}$. It can be observed that with these resolutions the solute profile is almost independent of Δx. In Table II we summarize the grid parameters we used in our simulations for each value of ϵ/δ.

TABLE II. Resolution of the computational grid at various ϵ/δ values.

ϵ/δ	Δx	Δt
0.025	8×10^{-4}	2×10^{-10}
0.050	8×10^{-4}	8×10^{-10}
0.100	8×10^{-4}	8×10^{-10}
0.200	4×10^{-4}	1.25×10^{-10}
0.500	4×10^{-4}	1.25×10^{-10}
1.000	4×10^{-4}	1.25×10^{-10}
$\infty(\delta=0)$	4×10^{-4}	1.25×10^{-10}

IV. NUMERICAL RESULTS

A. Growth in steady conditions

At first, we characterized the solidification process in steady conditions, determining the two constitutional laws $k(v)$ and $T_I(v)$ which describe the interface dynamics. We set $c_{-\infty}=0.056\,09$ in the solid phase, $c_{+\infty}=0.070\,68$ in the liquid phase, and $\overline{T_I}=1706.06$ K. Depending on the isotherm velocity, an oscillatory instability of the solidification front can arise when the imposed thermal gradient is not sufficiently high (see the next subsection). Then we chose $G=200$ K; with this value, after an initial transient, solidification proceeded at constant rate and with uniform concentration $c_{+\infty}$ in the solid phase. The solute segregation on the moving front was evaluated computing the minimum and maximum values c_s^* and c_l^* of the solute concentration across the interface and defining the partition coefficient as $k(v)=c_s^*/c_l^*$; the interface temperature was determined interpolating the temperature field at $x(\phi=0.5,t)$. Except for temperatures, all the results will be presented in nondimensional units; for the reader's commodity, we recall that the length scale is fixed at $\xi=2.1\times10^{-4}$ cm, and the resulting time and velocity scales are 4.41×10^{-3} s and 4.76×10^{-2} cm/s, respectively.

To compare our findings with the predictions of the continuous growth model, we recall that the latter gives the dependence of the partition coefficient on the growth velocity in the form

$$k(v)=\frac{k_e+v/v_d}{1+v/v_d}, \tag{19}$$

k_e being the equilibrium value for a stationary interface ($k_e=0.797$ in our case) and v_d the diffusional velocity for the solute redistribution across the moving front; v_d is generally expressed as $v_d=D/a$, where D is an interface diffusivity and a is the width of the concentration transition layer.

An asymptotic analysis of the phase-field model, conducted in the limit $\epsilon/\delta\ll1$ [5] pointed out that the partition coefficient scales, at large velocities, as $1-k(v)\sim v^{-2/3}$, unlike the predictions of the CGM which give $1-k(v)\sim v^{-1}$. However, our simulations were conducted with ϵ/δ ranging from 0.025 to ∞, so that we tried to identify in any case a characteristic velocity for solute trapping through a best fit of our numerical data with the dependence given by Eq. (19). The ratio ϵ/δ sets the length scale of the solute transition layer across the solid-liquid interface, opposing to the contraction of the solute profile. This issue is stressed in Fig. 2, where the solute field is shown for three different values of ϵ/δ; the isotherm velocity is $V_0=500$. The thickness of the transition layer is $l=24\times10^{-4}$ for $\delta=0$ and stretches to $l=70\times10^{-4}$ for $\epsilon/\delta=0.025$. Then we expect that solute relaxation across the interface becomes less effective at large velocities with decreasing ϵ/δ. Figure 3 shows the partition coefficient, normalized as $[k(v)-k_e]/(1-k_e)$, versus the interface velocity for different values of ϵ/δ. We observe that the curves corresponding to $\delta=0$ and $\epsilon/\delta=1.0$ are almost indistinguishable, but as ϵ/δ is further decreased, the partition coefficient shifts towards higher values and the onset of solute trapping occurs at lower interface velocities. Using v_d as an adjustable parameter in Eq. (19) to

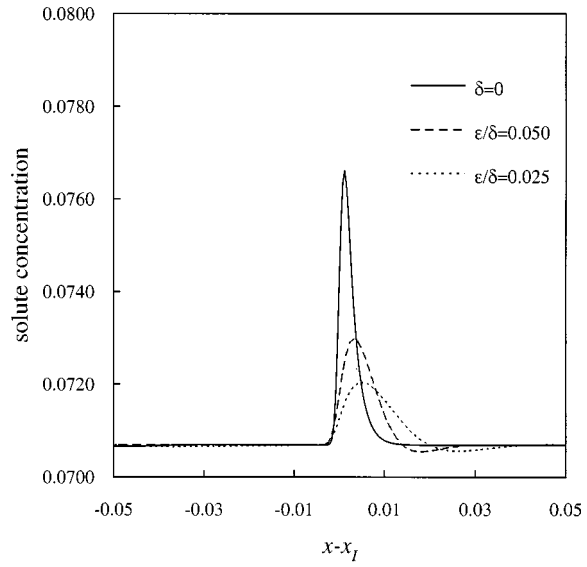

FIG. 2. Concentration profile for $V_0=500$ and $G=200$ K; x_I represents the position of the solid-liquid interface, located at $\phi=0.5$.

fit the data represented in Fig. 3, we obtained the results shown in Table III. The diffusional velocity corresponding to $\epsilon/\delta=0.025$ is more than an order of magnitude lower than the asymptotic value corresponding to $\delta=0$. It is worth noting that the available experimental data [15,16] indicate v_d values which never fall below the meter per second range, suggesting that the lowest values of ϵ/δ give an unrealistic picture of the solidification process.

The dependence of the interface temperature on the interface velocity is the result of two opposite effects. At low velocities, due to solute trapping (and to the consequent reduction of solute concentration on the liquid side of the interface), T_I is an increasing function of v. At higher velocities the undercooling required to advance the solidification front becomes important: the $T_I(v)$ curve traverses a maximum at $v=v^*$, $T=T^*$, and then exhibits a descending

TABLE III. Diffusional velocity v_d for different values of ϵ/δ.

ϵ/δ	v_d
0.025	25
0.050	55
0.100	110
0.200	190
0.500	265
1.000	285
∞	290

branch. Along these arguments the position of the maximum on the v axis should be strongly affected by the diffusional velocity v_d and, ultimately, by the ratio ϵ/δ. Figure 4 shows the numerical results for the $T_I(v)$ dependence. With increasing ϵ/δ the onset of solute trapping is shifted towards higher velocities and v^* is shifted as well. The latter is $v^*=200$ for $\epsilon/\delta=0.025$ and increases until $v^*=1400$ when $\delta=0$. On the other hand, the temperature T^* undergoes a variation of few tenths of degree over the whole range of variation of ϵ/δ. The above results suggest that phenomena critically dependent on v^* could be natural candidates to estimate the extent of the solute gradient correction in the model.

B. Oscillatory instability of the solidification front: The effect of the solute profile

The $T_I(v)$ curves shown in Fig. 4 exhibit a nonmonotonic behavior. In the range of positive slope the driving force for the process (i.e., the thermodynamic undercooling) is a decreasing function of the associate flux (the growth rate), resulting in unstable planar growth. When the isotherm velocity is fixed in this region and the thermal gradient is not sufficient for an effective restabilization, steady growth is prevented and the process undergoes periodic transitions between low- and high-velocity states [10,17–20]. This instability is responsible for the formation of the so-called *banded*

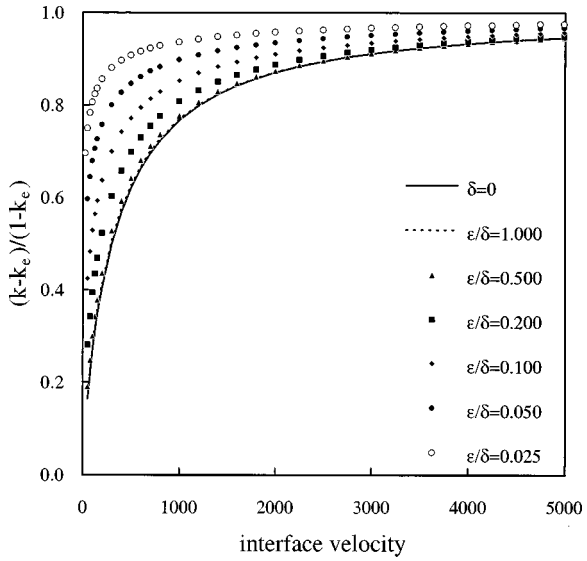

FIG. 3. Normalized partition coefficient versus the front velocity for different values of the ϵ/δ ratio.

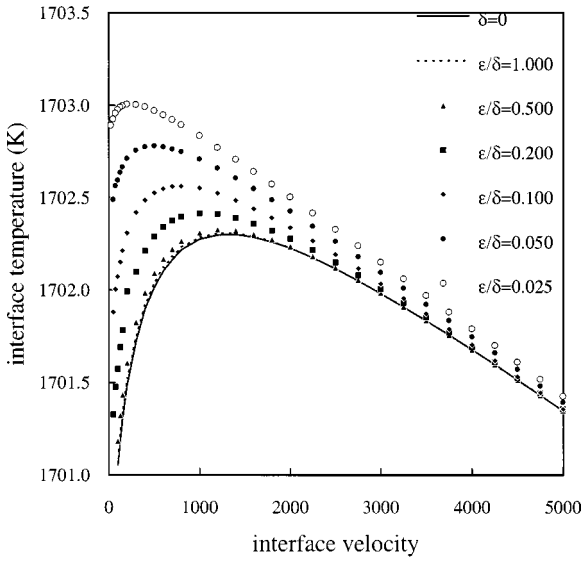

FIG. 4. Interface temperature versus the front velocity for different values of the ϵ/δ ratio.

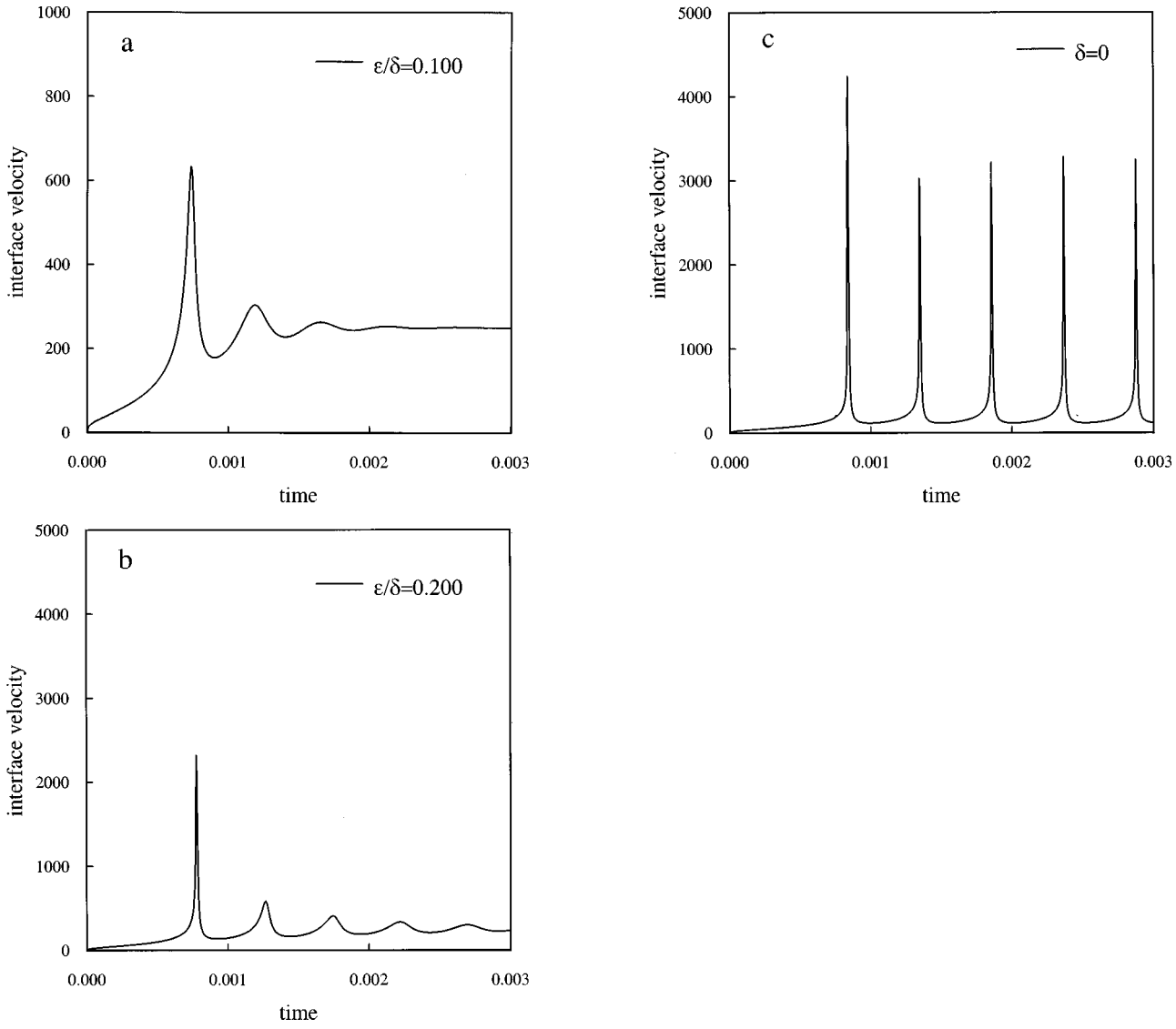

FIG. 5. Interface velocity vs time. The isotherm velocity is $V_0=250$ and the thermal gradient $G=40$ K. (a) $\epsilon/\delta=0.1$, (b) $\epsilon/\delta=0.2$, and (c) $\delta=0$.

structures. Observed by several authors in rapidly solidified alloys, at growth rates near the absolute stability limit, these structures consist of a regular succession of dark and light bands, parallel to the solid-liquid front, with a band spacing ranging from 0.3 to 1.5 μm. Detailed experimental studies [21–25] have shown that the dark bands have a precipitate structure, either cellular-dendritic or eutectic, depending on the alloy composition; the light bands are formed of precipitation-free solid solution, with a composition that is uniform and equal to the nominal concentration of the alloy.

As shown in Fig. 4, with increasing ϵ/δ the unstable (upsloping) branch of the $T_I(v)$ curves extends towards larger interface velocities, suggesting that the region of the parameters space where the oscillatory instability (and the banded structure) is expected should be strongly dependent on the ϵ/δ ratio. Plots of the interface velocity versus time are shown in Figs. 5(a)–5(c) for different values of ϵ/δ. The isotherm velocity is $V_0=250$ and the thermal gradient is $G=40$ K. When $\epsilon/\delta=0.1$ the effect of initial conditions is rapidly lost; the front velocity v (and the interface temperature T_I) describes few damped oscillations before reaching the final steady state with $v=V_0$. For $\epsilon/\delta=0.2$ the oscillations are still damped, but with a larger amplitude. A totally different dynamic behavior emerges when $\delta=0$. Here the isotherm velocity is fixed well inside the unstable branch; the process never reaches a steady regime, and the interface velocity continuously oscillates around the average value V_0. We observe, on the other hand, that the frequency of the oscillations [$\nu=1961$ in Fig. 5(c)] is almost unaffected by the ϵ/δ ratio.

The cyclic behavior of the interface dynamics shown in Fig. 5(c) is represented in Fig. 6 as an orbit followed by the system in the (T_I,v) plane (solid dots). The vertical line indicates the isotherm velocity $V_0=250$; on the same graph, the solid line represents the steady $T_I(v)$ curve. For most of the cycle, the interface velocity is lower than V_0 and the interface cools down; then, the orbit traverses the steady $T_I(v)$ curve at point A, where the front velocity is not far from V_0, and with a strong acceleration reaches point B on the stable branch. Here the interface velocity is much higher than V_0 and the interface warms up; solidification is decelerated and the operating point shifts to C. A numerical study

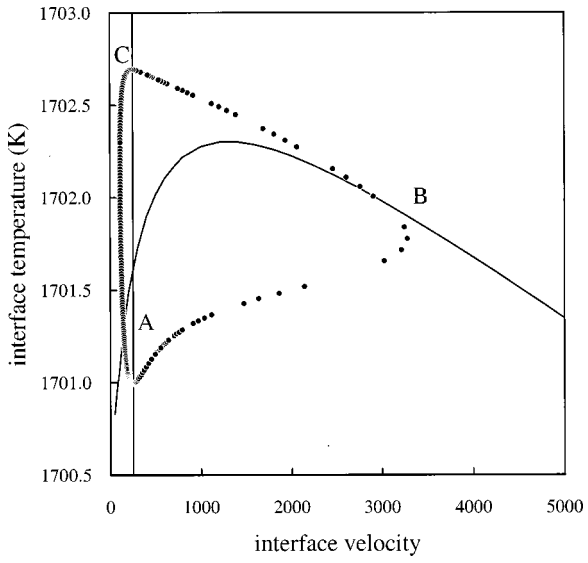

FIG. 6. Orbit followed by the process in the (T_I, v) plane for $\delta=0$. The isotherm velocity is indicated by the vertical line ($V_0=250$); $G=40$ K. The solid line indicates the steady $T_I(v)$ curve. The meaning of the points *A*, *B*, and *C* is illustrated in the text.

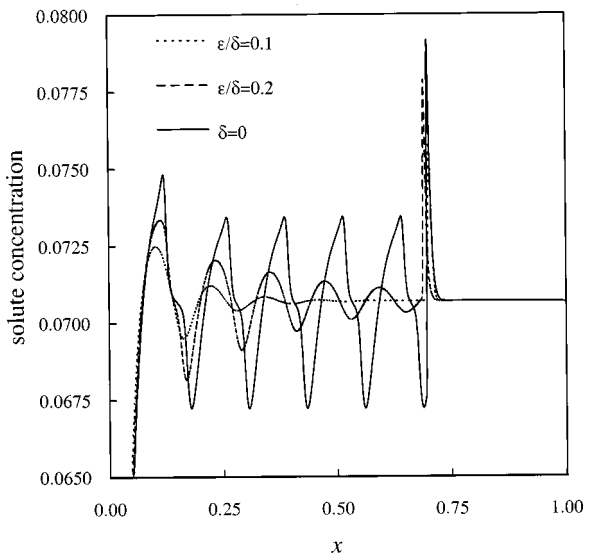

FIG. 7. Solute concentration profile along the growth direction for different values of the ϵ/δ ratio. The isotherm velocity is $V_0=250$ and the thermal gradient $G=40$ K.

conducted in two dimensions [26] showed that in the low-velocity section of the cycle the planar front breaks into a dendritic pattern, resulting in strong solute microsegregation; at high velocity, the absolute stability limit is reached, the dendritic pattern is suppressed, and planar growth occurs. Notice that the shape of the cycle can be modified when the latent heat diffusion is taken into account [18,27].

As the solute segregation across the interface depends on the interface velocity, we can argue that the extent of the concentration gradient correction should leave a trace in the solidified alloy. In Fig. 7 we show the concentration profile with $V_0=250$ and $G=40$ K. The solid-liquid interface is clearly recognizable at the peak of $c(x)$. For $\epsilon/\delta=0.1$ the concentration profile in the solid phase shows damped oscillations, along a distance corresponding to the initial transient; when the steady regime is reached, the composition of the solidified alloy corresponds to the liquid composition at infinity. For $\epsilon/\delta=0.2$ we observe that a distance of $x=0.5$ (corresponding to $x\sim 1$ μm) was not enough to reach the steady regime. When $\delta=0$ the periodic structure in the solid phase reflects the periodic variations of the interface velocity and temperature: at low velocity c_s reaches its minimum; then, the interface accelerates, solute partitioning is suppressed, and c_s increases. The wavelength of the solute concentration profile has been estimated as $\lambda=0.128$, which is practically coincident with the expected value $V_0/\nu=0.1274$.

V. CONCLUSIONS

In summary, we addressed the rapid directional solidification of a binary alloy through a phase-field model which includes gradient terms for both the order parameter and concentration field. To relate the extent of the gradient correction for the solute field to measurable quantities, we focussed on effects which are critically dependent on the composition across the solidification front. We found that the interface dynamics is almost unaffected when the ϵ/δ ratio changes from large values to $\epsilon/\delta\sim 1$: when δ is further increased until $\epsilon/\delta=0.025$, the diffusional velocity v_d is decreased by more than an order of magnitude; the interface temperature, on the other hand, is almost unaffected. The available experimental data, which indicate the onset of solute trapping in the meter per second range, suggest that small values of ϵ/δ give an unrealistic picture of the solidification process and should be discarded. The characteristic velocity v_d fixes also the range of interface velocities where the oscillatory instability of the solidification front is expected, as it reflects on the value of v^* which separates the stable and unstable branches of the steady $T_I(v)$ curve. At present, the evaluation of the growth rate in the banded structures is difficult, and experimental errors are greater than 20% [28]; however, the large excursion of v^* over the range of ϵ/δ values we explored in this paper should allow a reliable estimation of at least the order of magnitude of this parameter.

[1] Ch. Charach and B. Zaltzman, Phys. Rev. E **49**, 4322 (1994).
[2] Ch. Charach and Y. Keizman, in *Computational Modelling of Free and Moving Boundaries Problems*, edited by L. C. Wrobel, B. Sarler, and C. A. Brebbia (Computational Mechanics Publications, Southampton, England, 1995).
[3] M. J. Aziz and T. Kaplan, Acta Metall. **36**, 2335 (1988).
[4] M. J. Aziz and W. J. Boettinger, Acta Metall. Mater. **42**, 527 (1994).
[5] A. A. Wheeler, W. J. Boettinger, and G. B. McFadden, Phys. Rev. A **45**, 7424 (1992).

[6] G. Caginalp and J. Jones, Ann. Phys. (N.Y.) **237**, 66 (1995).
[7] A. A. Wheeler, W. J. Boettinger, and G. B. McFadden, Phys. Rev. E **47**, 1893 (1993).
[8] Zhiqiang Bi and Robert F. Sekerka, Physica A **261**, 95 (1998).
[9] Ch. Charach and P. C. Fife, in *Computational Modelling of Free and Moving Boundaries Problems*, edited by R. Van Keer and C. A. Brebbia (Computational Mechanics Publications, Southampton, England, 1997).
[10] M. Conti, Phys. Rev. E **56**, 3717 (1997).
[11] N. A. Ahmad, A. A. Wheeler, W. J. Boettinger, and G. B. McFadden, Phys. Rev. E **58**, 3436 (1998).
[12] J. A. Warren and W. J. Boettinger, Acta Metall. Mater. **43**, 689 (1995).
[13] S. L. Wang, R. F. Sekerka, A. A. Wheeler, B. T. Murray, S. R. Coriell, R. J. Braun, and G. B. McFadden, Physica D **69**, 189 (1993).
[14] R. Willnecker, D. M. Herlach, and B. Feuerbacher, Phys. Rev. Lett. **62**, 2707 (1989).
[15] K. Eckler, D. M. Herlach, and M. J. Aziz, Acta Metall. Mater. **42**, 975 (1994).
[16] P. M. Smith and M. J. Aziz, Acta Metall. Mater. **42**, 3515 (1994).
[17] M. Conti, Phys. Rev. E **58**, 2071 (1998).
[18] A. Karma and A. Sarkissian, Phys. Rev. Lett. **27**, 2616 (1992).
[19] A. Karma and A. Sarkissian, Phys. Rev. E **47**, 513 (1993).
[20] G. J. Merchant and S. H. Davis, Acta Metall. Mater. **38**, 2683 (1990).
[21] W. J. Boettinger, D. Shechtman, R. J. Schaefer, and F. S. Biancaniello, Metall. Trans. A **15**, 55 (1984).
[22] M. Zimmermann, M. Carrard, and W. Kurz, Acta Metall. **37**, 3305 (1989).
[23] M. Zimmermann, M. Carrard, M. Gremaud, and W. Kurz, Mater. Sci. Eng., A **134**, 1278 (1991).
[24] M. Gremaud, M. Carrard, and W. Kurz, Acta Metall. Mater. **38**, 2587 (1990).
[25] M. Carrard, M. Gremaud, M. Zimmermann, and W. Kurz, Acta Metall. Mater. **40**, 983 (1992).
[26] M. Conti, Phys. Rev. E **58**, 6101 (1998).
[27] M. Conti, Phys. Rev. E **58**, 6166 (1998).
[28] M. Gremaud, M. Carrard, and W. Kurz, Acta Metall. Mater. **39**, 1431 (1991).